Crystallographic Origin of Cycle Decay of the High-Voltage $LiNi_{0.5}Mn_{1.5}O_4$ Spinel Lithium-Ion Battery Electrode

Received 00th January 20xx,
Accepted 00th January 20xx

DOI: 10.1039/x0xx00000x

www.rsc.org/

Wei Kong Pang,[a,b] Cheng-Zhang Lu,[c] Chia-Erh Liu,[c] Vanessa K. Peterson,[*a] Hsiu-Fen Lin,[c,d] Shih-Chieh Liao,[c] and Jin-Ming Chen[c]

High-voltage spinel $LiNi_{0.5}Mn_{1.5}O_4$ (LNMO) is considered a potential high-power-density positive electrode for lithium-ion batteries, however, it suffers from capacity decay after extended charge-discharge cycling, severely hindering commercial application. Capacity fade is thought to occur through the significant volume change of the LNMO electrode occurring on cycling, and in this work we use *operando* neutron powder diffraction to compare the structural evolution of the LNMO electrode in an as–assembled 18650–type battery containing a $Li_4Ti_5O_{12}$ negative electrode with that in an identical battery following 1000 cycles at high-current. We reveal that the capacity reduction in the battery post cycling is directly proportional to the reduction in the maximum change of the LNMO lattice parameter during its evolution. This is correlated to a corresponding reduction in the MnO_6 octahedral distortion in the spinel structure in the cycled battery. Further, we find that the rate of lattice evolution, which reflects the rate of lithium insertion and removal, is ~ 9 and ~ 10% slower in the cycled than in the as–assembled battery during the Ni^{2+}/Ni^{3+} and Ni^{3+}/Ni^{4+} transitions, respectively.

Introduction

Lithium-ion batteries (LIBs) are the major power source for portable electronic devices, especially for use in automotive applications, following their first use with $LiCoO_2$ and graphite electrodes in 1991.[1] With developing technology requiring LIBs with energy and power capabilities that are beyond the existing state of the art, high-voltage electrodes for LIBs are an area of intense research. In the USA for example, only ~ 2% of the total energy use comes from personal electronics and ~ 67% from transportation and the grid, prompting the development of higher battery performance.[2] The performance characteristics required for such applications include long cycle life and high power/energy density, with widely-studied LIB electrode materials that lead to these performance characteristics including lithium-rich Ni-Mn-Co (NMC) type layered oxides containing a Li_2MnO_3 superstructure phase[3], mixed manganese-based spinels[4, 5], as well as Ni- and Co-based poly-anion materials[6]. In seeking improved performance characteristics such as a high insertion working voltage (~ 4.7 V vs. Li), high rate capability and energy density, other factors are also important and considered, including cost, safety, and environmental friendliness. With all these factors taken together, the $Ni_{0.5}Mn_{1.5}O_4$ (LNMO) spinel material is the most promising positive LIB electrode for such applications.[7]

LNMO can exist with $P4_332$ or $Fd\bar{3}m$ space-group symmetry.[8-11] The $P4_332$ spinel has ordered ionic arrangements of Li^+ at the 8*c* site, Ni^{2+} at the 4*b* site, Mn^{4+} at the 12*d* site, as well as O^{2-} at 8*c* and 24*e* sites. The $Fd\bar{3}m$ spinel has less ordered (disordered) arrangements, with Li^+ at 8*a* sites, Ni^{2+} and Mn^{4+} at 16*d* sites, and O^{2-} at 32*e* sites. It is generally accepted that disordered LNMO exhibits slightly better charge-discharge and cycling characteristics than the ordered phase, due to higher electronic conductivity and lower impedance.[12] Nevertheless, unfortunately, the cycle life of both spinel electrodes is poor and there is intense research underway to increase cycling performance.[4, 11-18]

The main challenges in this research are the stability of conventional organic carbonate-based electrolytes (< 4.3 V vs. Li)[19-24] at the required high voltage and the electrochemical two-phase behavior of the electrode.[9, 10, 25] The high voltage deterioration of the electrolyte induces the formation of a solid-electrolyte interphase (SEI) layer with low lithium conductivity at the electrode surface that hinders rate capability[5, 26] as well as causing the formation of HF, which corrodes the electrode and accelerates the dissolution of Mn into the electrolyte *via* disproportionation reactions.[24] These phenomena lead to poor cycling performance. In previous work, we showed that single–phase or solid-solution and two-phase reactions are associated with the Ni^{2+}/Ni^{3+} and Ni^{3+}/Ni^{4+} redox couples, respectively, in disordered LNMO.[9] Ariyoshi et al. reported that ordered LNMO undergoes two cubic-cubic two-phase reactions upon charging, accompanied by a 6% change in lattice volume.[27] It is well–known that, for insertion materials, cycle performance is closely connected to electrode structure. Importantly, the two-phase separation of LNMO causes the formation of Li–rich and Li–poor domains, similar to the "domino-cascade model" introduced by Delmas et al.[28],

[a] *Australian Nuclear Science and Technology Organisation, Locked Bag 2001, Kirrawee DC, NSW 2232, Australia.*
[b] *Institute for Superconducting & Electronic Materials, Faculty of Engineering, University of Wollongong, NSW 2522, Australia.*
[c] *Department of Energy Nanomaterials, Material and Chemical Research Laboratory, Industrial Technology Research Institute, Taiwan.*
[d] *Department of Materials Science and Engineering, National Formosa University, Yunlin County 63201, Taiwan.*
* Corresponding author.

Electronic Supplementary Information (ESI) available: X–ray and neutron powder diffraction data of LNMO powders used to make the electrodes for the 18650 batteries (Figure S1); charge–discharge history of cycled battery (Figure S2); Rietveld refinement profile using NPD data of the as–assembled battery (Figure S3); results of single–peak fitting of the LNMO 222 reflection in the NPD data (Figure S4); the variation of the oxygen positional parameter of the LTO phase (Figure S5); crystal structure of the LTO and LNMO powders used in the sequential refinement (Table S1). See DOI: 10.1039/x0xx00000x

inducing unfavorable inter-grain stress and breakdown of grain integrity through phase bordering and interface movement.[7] Consequently, this spinel electrode has a relatively poor cycle life compared to layered oxides that possess single–phase or solid-solution behavior in long-term cycling. Although the mechanism of cycle degradation of LNMO was hypothesized to occur though changes in phase volume during a two-phase electrochemical electrode behavior, prior to the present work there were no structure-function studies of LNMO detailing the degradation process. In this work we examine the structural evolution of LNMO in 18650–type batteries which also contain $Li_4Ti_5O_{12}$ (LTO) using *operando* neutron powder diffraction (NPD) during galvanostatic charge and discharge within the 2.0 – 3.5 V window (vs. LTO). We compare the structural evolution of LNMO in an as–assembled battery with that within a battery after 1000 cycles.

Experimental

LNMO powders were synthesized by a co-precipitation method. An aqueous solution of $NiSO_4 \cdot 6H_2O$ and $MnSO_4 \cdot H_2O$ was slowly pumped into a beaker at 50 °C, alongside aqueous solutions of NH_4OH and NaOH to maintain a pH of 10.5. $Ni_{0.25}Mn_{0.75}(OH)_2$ precursor with a particle diameter of approximately 10 – 15 μm was obtained from the co-precipitation process and mixed with lithium carbonate (Li_2CO_3) powder and calcined in air at 750 °C for 12 h to obtain $LiNi_{0.5}Mn_{1.5}O_4$. The co-precipitation process was scaled to produce 250 g, with 3 batches required to obtain enough LNMO active material for the battery. The X-ray diffraction and NPD data of the LNMO powders are shown in **Figure S1** in the ESI. LTO powder was purchased commercially from Ishihara Sanyo Kaisha, Ltd.

LNMO and LTO electrodes were prepared by casting a slurry of active material (80 wt.%), acetylene black (10 wt.%), and polyvinylidene difluoride (PVDF) binder (10 wt.%), dissolved in N-methyl pyrrolidinone (NMP), onto Al foil using a double-sided coating machine. The practical capacity of these electrodes within coin-cells was determined to be 140 and 150 mAh/g for LNMO and LTO, respectively. 18650–type batteries with Celgard® separator in an Al container were prepared by the Industrial Technology Research Institute (ITRI) of Taiwan and used in *operando* NPD studies. These batteries contained ~ 10.2 g LNMO electrode and ~ 8.1 g LTO electrode, yielding a maximum battery capacity of ~ 1.2 Ah as limited by the LTO, allowing the complete transformation of the LNMO to be observed.

Operando NPD data of batteries as–assembled and following 1000–cycles at 3C (cycle history is shown in **Figure S2**) were collected using WOMBAT,[29] the high-intensity neutron powder diffractometer at the OPAL research reactor at ANSTO, which features an area detector that continuously covers 120° in 2θ and has a relatively intense neutron beam, allowing the rapid collection of data. A neutron beam with wavelengths of 2.41646(8) and 2.41533(8) Å for the fresh and cycled batteries, respectively, were used, determined using the $La^{11}B_6$ NIST Standard Reference Material (SRM) 660b. The diffractograms were each obtained with a 1 min exposure time over the angular range 20 – 136.9° in 2θ during charge-discharge cycling. NPD data were collected while the batteries were cycled galvanostatically using a potentiostat/galvanostat (Autolab PG302N) at a current of 0.09 A (equivalent to 0.1C rate as suggested by preliminary testing) during charge, discharge, and a second charge, between 2.0 and 3.5 V (vs. LTO).

NPD data were analyzed using Fullprof with visualization in WinplotR,[30, 31] with Rietveld refinements performed using data in the range 30 – 110° in 2θ. Multi-peak fitting analysis of overlapping Al 111/LNMO 222 reflections were performed using Origin® and single–peak fitting analyses of overlapping Al 111/LNMO 222 reflections and LTO 222 were also performed using the Large Array Manipulation Program (LAMP).[32]

Results and discussion

Analysis of the X–ray diffraction and NPD data for the electrode powders (**Figure S1 and Table S1**) confirms the expected structure for these and reveals the main LNMO phase to be the ordered $P4_332$ symmetry type. To connect the cycling performance of the battery with the structural evolution of the LNMO electrode, high-intensity NPD data of as–assembled and cycled 18650–type batteries containing LNMO and LTO electrodes during charge and discharge were collected. **Figure 1** shows the charge-discharge profiles of the batteries during the *operando* NPD experiments. During the first (formation) cycle at 0.09 A, the as–assembled battery was over-charged to a capacity of 1.25 Ah and exhibited a Coulombic efficiency of 87.2%. In the second cycle, a charge capacity of 1.12 Ah and similar plateau-features to the formation cycle were observed. The absence of the ~ 2.45 V (vs. LTO) plateau arising from the Mn^{3+}/Mn^{4+} redox reaction (4 V vs. Li) indicates no oxygen deficiency in the LNMO structure or a disordered phase. This further supports the main phase of the LNMO being the ordered type with $P4_332$ space-group symmetry. The as–assembled battery was compared with a second battery that had been cycled 1000 times at high C rate (3C), during which significant capacity decay occurred (**Figure S2**). During the NPD experiment, the charge–discharge curve at 0.09 A for the cycled battery exhibited charge and discharge capacities of 0.92 and 0.77 Ah, respectively, followed by a charge capacity of 0.80 Ah, indicating a charge capacity that was ~ 29% smaller than the as–assembled battery (based on the second, non-formation cycle), with good reversibility of the charge–discharge cycle profile.

The NPD data of the batteries contains a significant background from the hydrogen–containing separator (Celgard®) and conventional protonated liquid electrolyte. Additionally, reflections from the Al current collector overlapped those from the LNMO and LTO electrodes, limiting the structural detail that could be obtained. Rietveld refinement plots using the NPD data of the batteries prior to electrochemical cycling in the *operando* NPD experiment are shown in **Figure S3**. There are, as expected, 3 identifiable phases in the battery: Al (current collectors and casing), LTO

(negative electrode), and LNMO (positive electrode). Prominent electrode peaks are the LTO 222 and LNMO 222 reflections, with the LNMO 222 overlapping with the Al 111 reflection (the Al lattice parameter ~ 4.0491 Å).

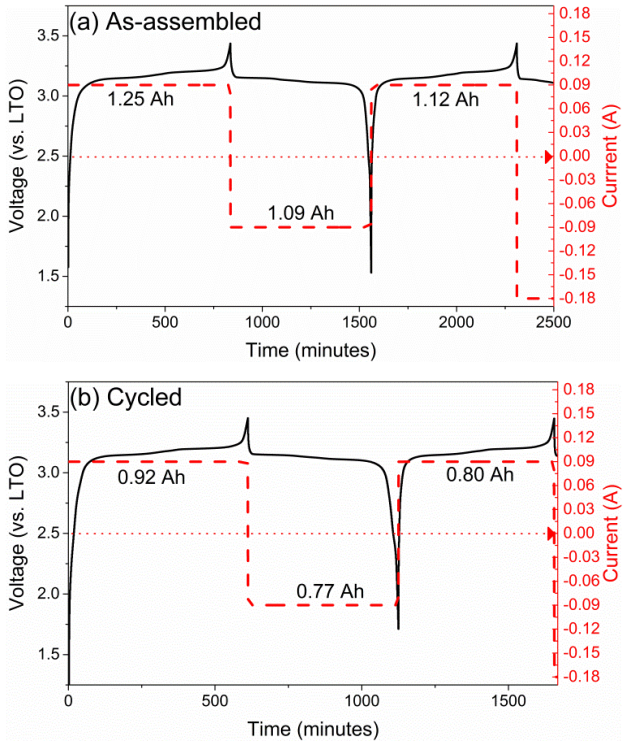

Figure 1. Charge–discharge profiles of (a) as–assembled and (b) cycled 18650–type batteries during the *operando* NPD measurement.

A select region of NPD data collected during the *operando* experiment, and corresponding to the charge–discharge behaviour in **Figure 1**, for the as–assembled and cycled battery are shown as a contour plot in **Figure 2a** and **2b,** respectively, where intensity is in colour. The background in the NPD data arises predominantly from the protonated electrolyte, and the stability of this during the course of the experiment for both batteries indicates a normal function, without decomposition, of the electrolyte, even during the 3.5 V vs. LTO charge (equivalent to ~ 5.05 V vs. Li). The structural behaviour of the negative electrode is captured by the changes in the LTO 222 reflection position and intensity. Changes in the position of this reflection during the experiment are relatively small for both batteries, as expected given the "zero–strain" property of the material. By comparison, there is a relatively-large change in intensity of this reflection, consistent with the changing population of lithium at the 16*c* crystallographic site.[33, 34] The structural behaviour of the positive electrode are captured in the NPD data by changes in the LNMO 222 reflection intensity and position, with this analysis being complicated by its overlap with the Al 111 reflection. Both the intensity and position of the LNMO 222 reflection change significantly during the NPD experiment for both batteries. The LNMO and LTO electrodes were treated as a single–phase during the experiment, by approximating the reaction of both electrodes as solid–solution during the sequential Rietveld refinement, with the LNMO modelled as the ordered $P4_332$ spinel structure, as described in **Table S1**.

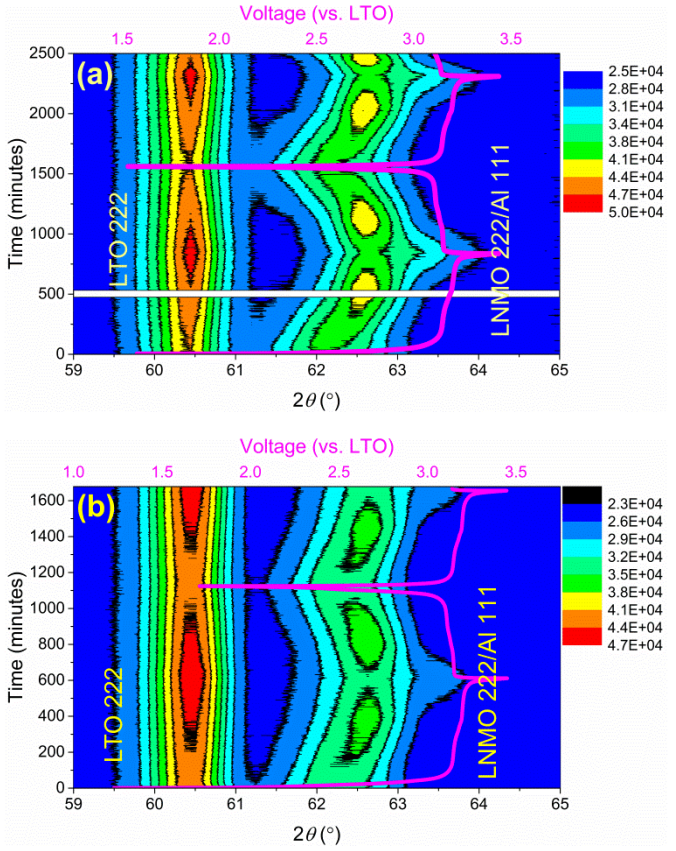

Figure 2. 2-dimensional intensity-contour plots of a selected 2θ region of *operando* NPD patterns for (a) as–assembled and (b) cycled batteries. Charge–discharge profiles are also shown overlaid.

The evolution of the LNMO lattice in the batteries obtained from Rietveld analysis of the NPD data are shown in **Figure 3**. Following Vegard's behaviour, the lattice parameter of LNMO decreases with delithiation and increases during lithium re-insertion. The overall change of the LNMO lattice parameter is correlated with battery capacity. For example, during the 1st discharge of the as–assembled battery the derived capacity of 1.09 Ah corresponds to a ~ 0.98% change in lattice parameter, and the corresponding 0.77 Ah capacity of the cycled battery corresponds to a 0.64% lattice change. The cycled battery therefore has a 1st discharge capacity that is ~ 29% less than the as–assembled battery and this corresponds to a ~ 35% lower overall change in the LNMO lattice parameter. Similarly, during the second charge the capacity of the cycled battery (0.80 Ah) is ~ 29% lower than the as–assembled battery (1.12 Ah), corresponding to a ~ 32% smaller change in LNMO lattice parameter. The lower capacity of the cycled than the as-assembled battery results in fewer lithium ions reversibly inserting into the electrode, and this is reflected consistently in its relatively-lower lattice parameter variation.

Linear fitting of the time evolution of the lattice parameter reveals its rate of change (**Figure 3**). The rate of change of the LNMO lattice during the Ni^{2+}/Ni^{3+} and Ni^{3+}/Ni^{4+} redox

transitions are different. These were 1.34 and 1.22 x 10^{-4} Å/min in the as–assembled and cycled batteries, respectively, for the Ni^{2+}/Ni^{3+} transition and 7.66 and 6.86 x 10^{-5} Å/min, respectively, for the Ni^{3+}/Ni^{4+} transition. These differences are correlated to differences in the ionic radii of the Ni ions (Ni^{2+} = 0.69 Å, Ni^{3+} = 0.56 Å, Ni^{4+} = 0.48 Å).[35] The corresponding rates of LNMO lattice change are ~ 9 and ~ 10% slower in the cycled than the as–assembled battery during the Ni^{2+}/Ni^{3+} and Ni^{3+}/Ni^{4+} transitions, respectively,

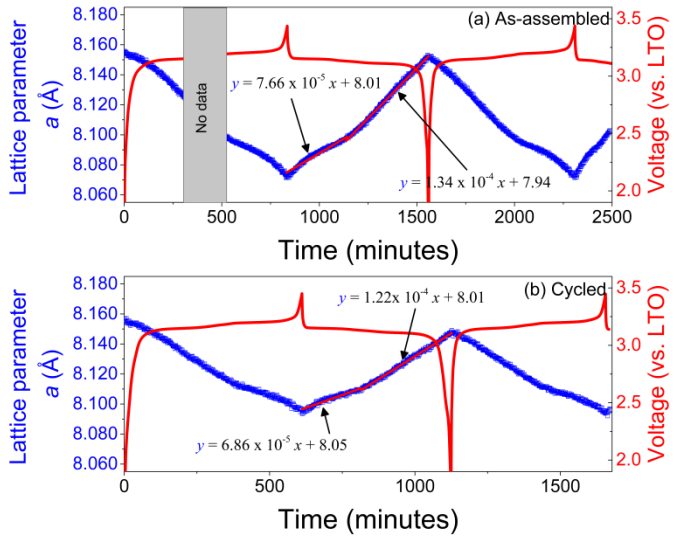

Figure 3. Lattice evolution of LNMO in (a) as–assembled and (b) cycled batteries.

To understand further the structural response of LNMO in the as–assembled and cycled batteries, peak fitting of overlapping LNMO 222 and Al 111 reflections was performed using two Gaussian functions and results shown in **Figure 4.** Given the inactive role of Al as both current collector and casing, no change in the Al 111 reflection position or intensity is expected, and the peak describing this reflection was therefore fixed during fitting process.

In the NPD data of the as–assembled battery the LNMO 222 reflection moves from 62.02(1) to 62.93(1)° on charge, returning to 62.04(1)° on discharge. A similar trend in the LNMO 222 reflection position is observed for the cycled battery, but this is smaller in magnitude, as expected given the lattice response and it being directly proportional to capacity, moving 0.60(2)°/Ah in the cycled battery compared with 0.73(2)°/Ah in the as–assembled battery.

Although the integrated intensity of the LNMO 222 reflection in the NPD data shows significant scatter and relatively-large error, overall the integrated intensity is at its highest at the high charge state (during the Ni^{3+}/Ni^{4+} transition), as shown more clearly for the as–assembled battery using a single–peak fitting approach (**Figure S4**, where an adequate fit to the NPD data of the cycled battery could not be obtained using a single–peak approximation). Again, the overall magnitude of the intensity change is significantly less for the cycled than the as–assembled battery.

The width of the LNMO 222 reflection also increases during the Ni^{3+}/Ni^{4+} transition, with the greatest peak broadening in NPD data of both the as–assembled and cycled batteries corresponding to the highest intensity of this reflection. Ariyoshi et al[27] described a two two–phase reaction mechanism of LNMO, involving a Li-poor phase with lattice parameters that would position this reflection near its maximum of 62.93(1)° observed in our solid–solution approximation, implying the occurrence of a two-phase reaction mechanism. Interestingly, the magnitude of broadening of this reflection is similar for both as–assembled and cycled batteries, suggesting that mechanistically the LNMO is undergoing a similar two-phase evolution.

Figure 5 shows the refined LNMO structures at open-circuit voltage (OCV) and charged state in the as–assembled and cycled batteries. Structural distortion is clearly observed in response to delithiation to absorb the lattice strain. **Table 1** summarises the bond length and angles and their % change on delithiation (between the OCV/rest and charged battery states). The main distortion is found to occur around the MnO_6 octahedra, although this distortion is significantly less in the cycled than in the as–assembled battery, consistent with the proportionally reduced change in lattice as correlated with the reduced capacity.

Figure 6 shows the evolution of LTO lattice and LTO 222 single peak fit parameters for NPD data of the as–assembled and cycled batteries. Between the at rest or OCV battery state and the charged state of 3.5 V vs. LTO, the LTO lattice parameter changed by a maximum of only 0.011(2)% and 0.004(1)% for the as–assembled and cycled batteries, respectively. In the as–assembled battery (**Figure 6a**), the LTO 222 reflection exhibits the largest change of 0.04(2)°, and revealing an initial shift to smaller angles as a consequence of lithium occupation at the 32*e* site during initial lithiation as shown previously.[9, 33, 34] In terms of LTO structure, the overall change in the positional parameter (x = y = z) of the oxygen atom is the same between the as–assembled and cycled batteries (**Figure S5**), the maximum being 0.006(1) (~ 2.4%). The LTO 222 reflection width increases slightly on charge, supporting the possibility of a two-phase reaction during lithiation of $Li_4Ti_5O_{12}$ to $Li_7Ti_5O_{12}$. As the latter lattice is only slightly smaller than the former,[36, 37] the separation of these phases (< 0.04°) is not possible at the resolution of the data (FWHM ~ 0.8°). Therefore, the LTO phase transition is modelled as a single–phase (solid–solution reaction) after Wagemaker et al,[38] the details of which are presented in **Table S1**.

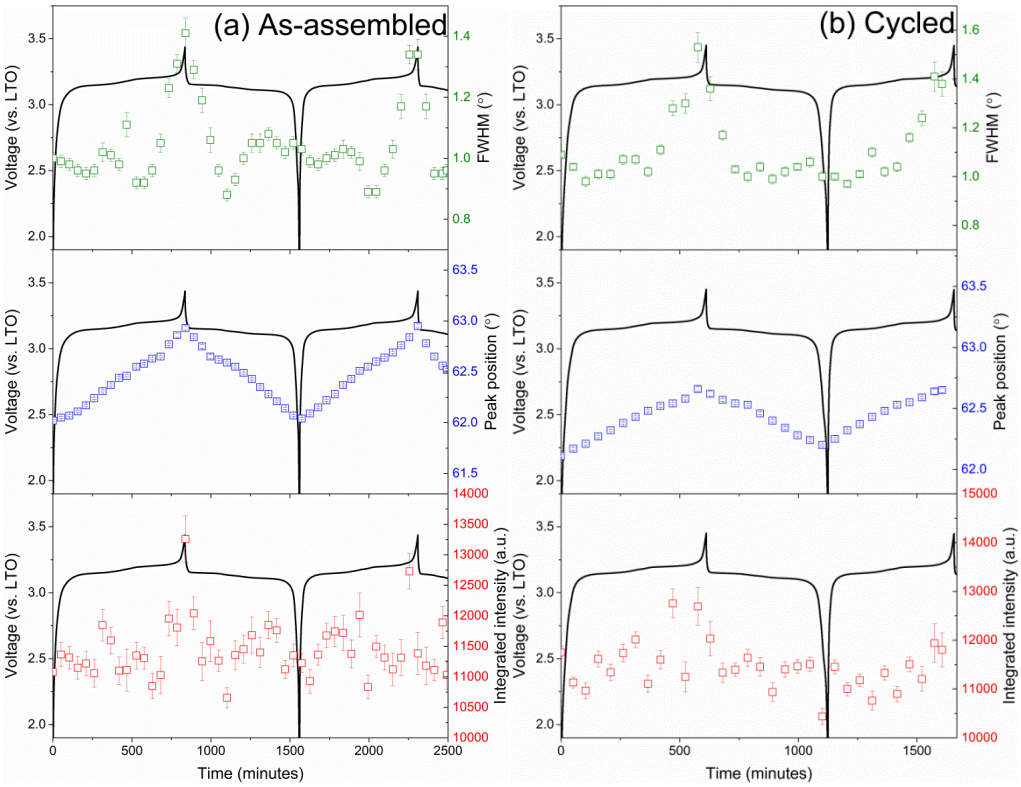

Figure 4. The integrated intensity (red), position (blue), and full width at half maximum (FWHM, green) of the peak describing the LNMO 222 reflection in *operando* NPD data of the (a) as–assembled and (b) cycled battery. Battery voltage is also shown.

As expected, the evolution of the refined lattice parameter correlated well with that of the LTO 222 reflection position. Although the reflection intensity correlated well with lithium content, increasing during lithiation and decreasing during de–lithiation, the determination of lithium occupation at crystallographic sites was not possible from these NPD data.

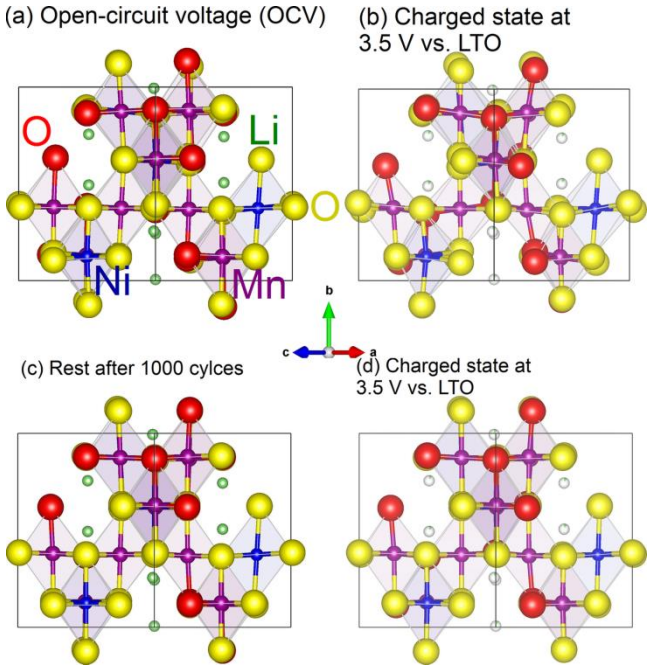

Figure 5. Crystal structure of LNMO in as–assembled (a and b) and cycled (c and d) batteries at OCV and rest (a and c), and charged state (b and d). Mn is shown in purple, Ni in blue, Li in green, and O in red (8*c* site) and yellow (24*e* site).

Table 1. Bond length and angles between Ni/Mn and O in LNMO at rest or OCV and charged states, for the as–assembled (blue) and cycled (red) batteries. O1 = O at the 8*c* site and O2 = O at the 24*e* site.

	Bond length (Å)			Bond angle (°)			
	Mn-O1	Ni-O2	Mn-O2	O1-Mn-O1	O1-Mn-O2	O2-Mn-O2	O2-Ni-O2
OCV	2.075(2)	2.047(2)	2.008(4)	88.287(3)	91.281(2)	93.015(4)	92.347(3)
Charged	1.829(2)	2.053(3)	1.822(2)	105.477(3)	77.873(2)	88.801(1)	103.917(3)
Approx. Change (%)	-11.9	0	-9.3	19.5	-14.7	-4.5	12.5

	Bond length (Å)			Bond angle (°)			
	Mn-O1	Ni-O2	Mn-O2	O1-Mn-O1	O1-Mn-O2	O2-Mn-O2	O2-Ni-O2
At rest	1.954(2)	2.044(2)	2.009(2)	95.293(4)	92.671(1)	94.666(7)	94.666(3)
Charged	1.917(2)	2.043(3)	2.084(2)	97.914(3)	93.785(2)	90.467(2)	94.582(5)
Approx. Change (%)	-1.9	0	3.7	2.8	1.2	-4.4	0

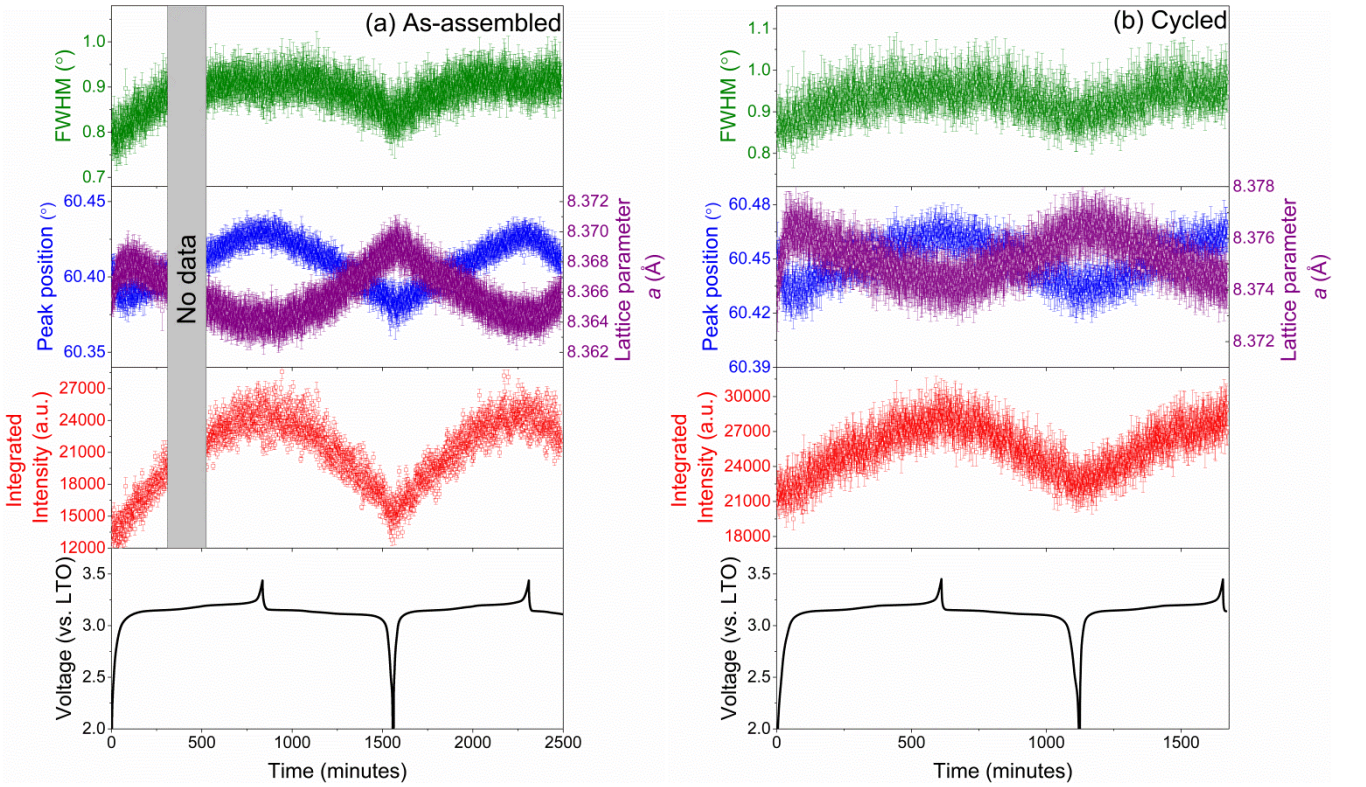

Figure 6. Evolution of single–peak fitting parameters of the LTO 222 reflection with intensity (red), position (blue), and full width at half-maximum (FWHM, green) using NPD data for (a) as–assembled and (b) cycled batteries. Refined lattice parameter and battery voltage are also shown.

Conclusions

Operando neutron powder diffraction (NPD) of 18650–type batteries containing $LiNi_{0.5}Mn_{1.5}O_4$ (LNMO) and $Li_4Ti_5O_{12}$ (LTO) electrodes was employed to investigate the structural evolution of the LNMO, responsible for capacity fade. The *operando* NPD study compared the evolution of the LNMO structure in as–assembled (fresh) and fatigued (following 1000 high–current cycles) batteries. Results point to a phase evolution of the LNMO electrode that is mechanistically the same in both batteries. Capacity fade of the cycled battery is directly proportional to the reduction in the overall change of the LNMO lattice parameter during its two phase evolution to a lithium poor phase. This is accompanied by a reduction in the MnO_6 octahedral distortion in the cycled battery. Lithium insertion and removal is reflected in the rate of lattice evolution, which is ~ 9 and ~ 10% slower in the cycled than the as–assembled battery during the Ni^{2+}/Ni^{3+} and Ni^{3+}/Ni^{4+} transitions, respectively.

Acknowledgements

The authors thank Bragg Institute operations support staff.

References

1. Y. Nishi, *J. Power Sources*, 2001, **100**, 101-106.
2. G. Crabtree, E. Kócs and L. Trahey, *MRS Bull.*, 2015, **40**, 1067-1078.
3. Y. Xiang, Z. Yin and X. Li, *Ionics*, 2014, **20**, 157-162.
4. P. Axmann, G. Gabrielli and M. Wohlfahrt-Mehrens, *J. Power Sources*, 2016, **301**, 151-159.
5. Y. Talyosef, B. Markovsky, G. Salitra, D. Aurbach, H. J. Kim and S. Choi, *J. Power Sources*, 2005, **146**, 664-669.
6. H. Li, Y. Wang, X. Yang, L. Liu, L. Chen and J. Wei, *Solid State Ionics*, 2014, **255**, 84-88.
7. A. Kraytsberg and Y. Ein-Eli, *Adv. Energy Mater.*, 2012, **2**, 922-939.
8. D. Pasero, N. Reeves, V. Pralong and A. R. West, *J. Electrochem. Soc.*, 2008, **155**, A282-A291.
9. W. K. Pang, N. Sharma, V. K. Peterson, J.-J. Shiu and S.-H. Wu, *J. Power Sources*, 2014, **246**, 464-472.
10. L. Cai, Z. Liu, K. An and C. Liang, *J. Mater. Chem. A*, 2013, **1**, 6908-6914.
11. J. H. Kim, S. T. Myung, C. S. Yoon, S. G. Kang and Y. K. Sun, *Chem. Mater.*, 2004, **16**, 906-914.
12. X. Y. Feng, C. Shen, X. Fang and C. H. Chen, *J. Alloy Compd.*, 2011, **509**, 3623-3626.
13. Y.-F. Deng, S.-X. Zhao, Y.-H. Xu and C.-W. Nan, *J. Power Sources*, 2015, **296**, 261-267.
14. Y. Fan, J. Wang, Z. Tang, W. He and J. Zhang, *Electrochim. Acta*, 2007, **52**, 3870-3875.

15. J.-C. Fang, Y.-F. Xu, G.-L. Xu, S.-Y. Shen, J.-T. Li, L. Huang and S.-G. Sun, *J. Power Sources*, 2016, **304**, 15-23.
16. X. Fang, M. Ge, J. Rong and C. Zhou, *J. Mater. Chem. A*, 2013, **1**, 4083-4088.
17. Y.-J. Gu, Y. Li, Y. Fu, Q.-F. Zang, H.-Q. Liu, J.-X. Ding, Y.-M. Wang, H.-F. Wang and J. Ni, *Electrochim. Acta*, 2015, **176**, 1029-1035.
18. M. C. Kim, S. H. Kim, V. Aravindan, W. S. Kim, S. Y. Lee and Y. S. Lee, *J. Electrochem. Soc.*, 2013, **160**, A1003-A1008.
19. S. Tan, Y. J. Ji, Z. R. Zhang and Y. Yang, *ChemPhysChem*, 2014, **15**, 1956-1969.
20. K. Kanamura, *J. Power Sources*, 1999, **81–82**, 123-129.
21. J. B. Goodenough and K.-S. Park, *J. Am. Chem. Soc.*, 2013, **135**, 1167-1176.
22. J. B. Goodenough and Y. Kim, *J. Power Sources*, 2011, **196**, 6688-6694.
23. J. B. Goodenough and Y. Kim, *Chem. Mater.*, 2010, **22**, 587-603.
24. L. Yang, B. Ravdel and B. L. Lucht, *Electrochem. Solid-State Lett.*, 2010, **13**, A95-A97.
25. K. Ariyoshi, Y. Iwakoshi, N. Nakayama and T. Ohzuku, *J. Electrochem. Soc.*, 2004, **151**, A296-A303.
26. H. Duncan, D. Duguay, Y. Abu-Lebdeh and I. J. Davidson, *J. Electrochem. Soc.*, 2011, **158**, A537-A545.
27. K. Ariyoshi, Y. Iwakoshi, N. Nakayama and T. Ohzuku, *J. Electrochem. Soc.*, 2004, **151**, A296-A303.
28. C. Delmas, M. Maccario, L. Croguennec, F. Le Cras and F. Weill, *Nat Mater*, 2008, **7**, 665-671.
29. A. J. Studer, M. E. Hagen and T. J. Noakes, *Physica B*, 2006, **385–386, Part 2**, 1013-1015.
30. J. Rodríguez-Carvajal, *Physica B*, 1993, **192**, 55-69.
31. T. Roisnel and J. Rodriguez-Carvajal, *Materials Science Forum, Proceedings of the Seventh European Powder Diffraction Conference (EPDIC 7)*, 2000, 118-123.
32. D. Richard, M. Ferrand and G. J. Kearley, *J. Neutron Res.*, 1996, **4**, 33-39.
33. W. K. Pang, V. K. Peterson, N. Sharma, J.-J. Shiu and S.-h. Wu, *Chem. Mater.*, 2014, **26**, 2318-2326.
34. W. K. Pang, V. K. Peterson, N. Sharma, J.-J. Shiu and S.-h. Wu, *Powder Diffr.*, 2014, **29**, S59-S63.
35. R. Shannon, *Acta Crystallogr. Sect. A*, 1976, **32**, 751-767.
36. S. Panero, P. Reale, F. Ronci, B. Scrosati, P. Perfetti and V. Rossi Albertini, *Phys. Chem. Chem. Phys.*, 2001, **3**, 845-847.
37. S. Scharner, W. Weppner and P. Schmid-Beurmann, *J. Electrochem. Soc.*, 1999, **146**, 857-861.
38. M. Wagemaker, D. R. Simon, E. M. Kelder, J. Schoonman, C. Ringpfeil, U. Haake, D. Lützenkirchen-Hecht, R. Frahm and F. M. Mulder, *Adv. Mater.*, 2006, **18**, 3169-3173.